European Rotorcraft Forum

CORRELATION OF FINITE STATE MULTI-ROTOR DYNAMIC INFLOW MODELS WITH A HIGH FIDELITY VISCOUS VORTEX PARTICLE METHOD

Feyyaz Guner feyyazguner@gatech.edu
J. V. R. Prasad jvr.prasad@ae.gatech.edu
Lakshmi N. Sankar lsankar@ae.gatech.edu
School of Aerospace Engineering
Georgia Institute of Technology
Atlanta, Georgia, USA

David Peters dap@wustl.edu
Mechanical Eng. & Materials Sci.
Washington University
Saint Louis, Missouri, USA

Chengjian He he@flightlab.com
Advanced Rotorcraft Technology, Inc.
Sunnyvale, CA, USA

Abstract
Finite state inflow models have been developed from potential flow theory to predict inflow distributions for single rotor configurations. Superposition of velocity or pressure potentials associated with individual rotors has been proposed for arriving at inflow models for multi-rotor configurations. In this study, fidelity assessment of finite state inflow models arrived at using pressure and velocity potential superposition methods for two tandem rotor configurations is considered. Physical wake effects, such as wake contraction and viscous wake dissipation, that are not inherently included in potential flow theory are added to both Pressure Potential Superposition Inflow Model (PPSIM) and Velocity Potential Superposition Inflow Model (VPSIM). In addition, new mass flow parameter formulation for VPSIM is proposed to match with one used in PPSIM. Using this formulation, it is shown that PPSIM and VPSIM have similar steady-state inflow distributions. For model fidelity assessment, the developed finite state inflow models are compared against a high fidelity numerical model known as Viscous Vortex Particle Method (VVPM). Differences in rotors uniform, fore-to-aft and side-to-side inflow components between the models are quantitatively analyzed in hover and forward flight. Contour plots of inflow distributions are also provided for qualitative comparison. In addition, effects of inflow distribution and interference velocities on flapping angle predictions are discussed.

1. NOMENCLATURE

L_q	Blade sectional circulatory lift, lbf/ft
M, N	Total number of harmonics and radial terms
Q	Number of blades on one rotor
R	Rotor radius, ft
$[L], [\tilde{L}]$	Influence coefficient matrix
$[M], [\tilde{M}]$	Apparent mass matrix
$[V_m]$	Mass flow parameter
$[\tilde{D}]$	Damping matrix
$\bar{P}_n^m$	Normalized Legendre function of the first kind
$\bar{r}$	Normalized blade radial coordinate
$\bar{v}_z$	Induced inflow normalized by blade tip speed
$\boldsymbol{v}$	Induced velocity vector
a_j^{rc}, a_j^{rs}	Velocity states corresponding to cosine and sine components, respectively
r, j	Harmonic and polynomial numbers, respectively
$\Delta_j^{rc}, \Delta_j^{rs}$	Adjoint velocity states corresponding to cosine and sine components, respectively

Ψ_n^m	Inflow shaping function
$\alpha_j^{rc}, \alpha_j^{rs}$	Pressure potential inflow states corresponding to cosine and sine components, respectively
$\bar{\psi}_q$	Azimuth angle of the qth blade
$\hat{\Psi}_n^{mc}, \hat{\Psi}_n^{ms}$	Cosine and sine components of the velocity potentials
τ_n^{mc}, τ_n^{ms}	Pressure coefficients of cosine and sine components
$\tilde{\Psi}_n^{mc}, \tilde{\Psi}_n^{ms}$	Cosine and sine components of the velocity shaping function
$(\,)_U, (\,)_L$	Related to upper/front and lower/back rotors, respectively
PPSIM	Pressure Potential Superposition Inflow Model
VPSIM	Velocity Potential Superposition Inflow Model
VVPM	Viscous Vortex Particle Method

2. INTRODUCTION

Accurate predictions of rotor inflows are necessary for performance, aeromechanics and handling qualities analyses of single and/or multi-rotor configurations. For single rotor configurations, finite state inflow models have been shown to have good correlations with experimental data[1,2,3]. Recent extension of pressure potential finite state inflow model to coaxial rotor configurations has shown that finite state inflow models capture the fundamental interference effects between rotors, and further improvements can be made by identifying any missing interference effects that are not inherently captured in a potential flow formulation[4,5,6,7,8,9]. Promising results for coaxial rotor configurations have led to generalization of the pressure and velocity potential superposition framework for application to multi-rotor configurations[10,11].

In this study, subsets of the multi-rotor finite state inflow models are used to estimate inflow prediction of two tandem rotor configuraions with different longitudinal separation distances. Moreover, previously identified missing wake contraction and viscous dissipation effects[11] are added to both pressure potential superposition inflow (PPSIM) and velocity potential superposition inflow (VPSIM) models. The mass flow parameter calculation of VPSIM model is revisited[11], and a new formulation closer to the classical approach is proposed.

The main objective of this paper is to compare pressure potential superposition and velocity potential superposition inflow models againts a high fidelity viscous Vortex Particle Method (VVPM)[12] for tandem rotor configurations. In this work, VVPM is considered as 'truth' model. Obtained steady-state inflow distributions are reduced to uniform, fore-to-aft and side-to-side inflow components for quantitative comparison at low and high speed conditions. In addition, contour plots of inflow distributions are provided to qualitatively identify the discrepancies in the rotors induced inflow distributions. The differences among the models are identified and new corrections are proposed for further improvement. Lastly, effects of inflow distribution and interference velocities on flapping angle predictions are presented.

3. FINITE STATE INFLOW MODELS

Pressure and velocity potential superposition inflow models assume that flow around the rotor disk is incompressible and inviscid. Although PPSIM and VPSIM assume rigid skewed wake geometry, in this work, wake geometry is modified to account for wake contraction effect. In this section, finite state inflow models for tandem rotor configurations are briefly described.

3.1. Pressure Potential Superposition Inflow Model (PPSIM)

In PPSIM, rotors' individual pressure fields can be superimposed. Then, governing inflow equation for tandem rotor configurations can be obtained as[11],

$$\begin{bmatrix} M_{11} & M_{12} \\ M_{21} & M_{22} \end{bmatrix} \begin{Bmatrix} \overset{*}{\alpha}_1 \\ \overset{*}{\alpha}_2 \end{Bmatrix} + \begin{bmatrix} V_{m1} & 0 \\ 0 & V_{m2} \end{bmatrix} \times \begin{bmatrix} L_{11} & L_{12} \\ L_{21} & L_{22} \end{bmatrix}^{-1} \begin{Bmatrix} \alpha_1 \\ \alpha_2 \end{Bmatrix} = \begin{Bmatrix} \tau_1/2 \\ \tau_2/2 \end{Bmatrix} \tag{1}$$

In equation (1), diagonal blocks (M_{11}, M_{22}, L_{11}, L_{22}) are related to self-induced effects while off-diagonal blocks (M_{12}, M_{21}, L_{12}, L_{21}) capture aerodynamic interference effects caused by the other rotor. Elements in each of these blocks are precalculated[10,11] numerically and tabulated. The flow parameter matrix, $[V_m]$ in equation (1) is diagonal since it is related to flow passing through each individual rotor. Note that subscripts "1" and "2" in α and τ refer to upper/front and lower/back rotors, respectively.

Elements in the mass flow parameter (V_T and V) can be obtained using uniform inflow state of each rotor, inplane (μ) and normal (λ_f) components of

free-stream velocity[2]. For example, mass flow parameter of rotor-1 becomes

$$
\begin{aligned}
V_{T1} &= \sqrt{\mu^2 + (\lambda_f + \lambda_{m1})^2} \\
V_1 &= \frac{\mu^2 + (\lambda_f + 2\lambda_{m1})(\lambda_f + \lambda_{m1})}{V_{T1}} \\
\lambda_{m1} &= \sqrt{3}\alpha_1(1)
\end{aligned} \tag{2}
$$

where $\alpha_1(1)$ is the first element of column vector of inflow states corresponding to rotor-1.
In PPSIM, wake contraction effects are taken into account by correcting the streamline coordinates when computing elements in the L-matrix[4]. In addition, an exponential wake decay function[4,13] is used to account for viscous wake decay. The function is given as,

$$V_{decay}(d) = V e^{(-d\zeta)} \tag{3}$$

where d is the distance of the flow field point of interest from the center of the source rotor that generates the interference and ζ is the empirical decay coefficient.

3.2. Velocity Potential Superposition Inflow Model (VPSIM)

Velocity potential finite state inflow model allows calculation of induced velocity both at a rotor disk and above the disk. In this model, induced velocity is expressed as gradient of summation of the cosine and sine part of the velocity potentials as shown in equation (4).

$$\boldsymbol{v} = \sum_{r=0}^{M} \sum_{j=r}^{N} \nabla(\hat{\Psi}_j^{rc} + \hat{\Psi}_j^{rs}) \tag{4}$$

Each velocity potential consists of time and spatial dependent parts, i.e. velocity states (a_j^r) for time dependency and velocity shaping function ($\tilde{\Psi}_j^r$) for spatial dependency.
Using the superposition approach, single rotor velocity potential inflow model has been extended to multi-rotor configurations by combining the velocity potentials to form Velocity Potential Superposition Inflow Model (VPSIM)[11]. For tandem rotor configuration, VPSIM takes the following form.

$$[\hat{M}]^* \begin{Bmatrix} \overset{*}{a}_1 \\ \overset{*}{\Delta}_1 \\ \overset{*}{a}_2 \\ \overset{*}{\Delta}_2 \end{Bmatrix} + [\hat{D}][V_m][\hat{L}]^{-1}[\hat{M}] \begin{Bmatrix} a_1 \\ \Delta_1 \\ a_2 \\ \Delta_2 \end{Bmatrix} = [\hat{D}] \begin{Bmatrix} \tau_1 \\ \tau_1^* \\ \tau_2 \\ \tau_2^* \end{Bmatrix} \tag{5}$$

where

$$
\begin{aligned}
[\hat{M}]^* &= diag(\tilde{M}_{11}, -\tilde{M}_{11}, \tilde{M}_{22}, -\tilde{M}_{22}) \\
[\hat{M}] &= diag(\tilde{M}_{11}, \tilde{M}_{11}, \tilde{M}_{22}, \tilde{M}_{22}) \\
[\hat{D}] &= diag(\tilde{D}_{11}, \tilde{D}_{11}, \tilde{D}_{22}, \tilde{D}_{22}) \\
[V_m] &= diag(V_{m11}, V_{m11}, V_{m22}, V_{m22}) \\
[\hat{L}] &= diag(\tilde{L}_{11}, \tilde{L}_{11}, \tilde{L}_{22}, \tilde{L}_{22})
\end{aligned}
$$

It is important to recognize that in VPSIM, each rotor has its own velocity potential. Therefore, velocity potentials of the rotors are superimposed to account for interaction between the rotors. Then, velocity vector at any desired location can be calculated using equation (6).

$$\boldsymbol{v} = \sum_{r=0}^{M} \sum_{j=r}^{N} \nabla[(\hat{\Psi}_j^r)_1 + (\hat{\Psi}_j^r)_2] \tag{6}$$

In this equation, $(\hat{\Psi}_j^r)_1$ and $(\hat{\Psi}_j^r)_2$ represent velocity potentials (include both sine and cosine parts) of rotor-1 and rotor-2, respectively. These velocity potentials consist of velocity states and shaping functions. In VPSIM, velocity states are modified to include viscous wake decay effect, and streamline coordinates of shaping functions are corrected based on the wake contraction effect. If desired location is inside the wake of a rotor, then adjoint velocity states of that rotor are also required. In this study, only 'z' component of the induced velocity is considered.

3.3. Mass Flow Parameter Matrix, $[V_m]$ and Skew Angle, χ in VPSIM

In tandem rotor configuration, net flow passing through the rotors must be corrected due to coupling effects. It has been shown that mass flow parameter has an effect on inflow distributions[11]. Aerodynamics interactions not only affect the elements in mass flow parameter matrix, V_T and V, they also affect the momentum theory wake skew angle, χ.
The different modeling structure of VPSIM prevents it having the same analytical mass flow parameter matrix with PPSIM. In PPSIM, both self and interference average induced velocities are available in analytical form. On the other hand, only average self induced velocity is analytically known in VPSIM; hence average interference velocities are numerically calculated. Sample calculations of V_T, V and χ for rotor-1 are given in equation (7).

$$V_{T1} = \sqrt{\mu^2 + (\lambda_f + \overline{v_z}_1 + \overline{v_z}_{12})^2}$$

$$V_1 = (\mu^2 + (\lambda_f + \overline{v_z}_1 + \overline{v_z}_{12}))\times (\lambda_f + 2(\overline{v_z}_1 + \overline{v_z}_{12}))/V_{T1} \quad (7)$$

$$\chi_1 = \frac{\pi}{2} - \tan^{-1}\left|\frac{\lambda_f + \overline{v_z}_1 + \overline{v_z}_{12}}{\mu}\right|$$

where, μ is normalized inplane velocity parallel to tip path plane and λ_f is the normalized velocity perpendicular to it, $\overline{v_z}_1$ is rotor-1 on disk average velocity and $\overline{v_z}_{12}$ is average interference velocity on rotor-1 due to rotor-2. The self induced average velocity, $\overline{v_z}_1$, is calculated using classic mass flow parameter equation[2] by transforming velocity state to Nowak-He variable.

$$\overline{v_z}_1 = \sqrt{3}a_{1NH}(1) \qquad a_{1NH} = [A]a_1 \quad (8)$$

where $[A]$ is the Nowak-He transformation matrix[15]. It is important to note that mass flow parameters of VPSIM and PPSIM are calculated using different approaches. Numerical estimations of average interference velocity ($\overline{v_z}_{12}$) is slightly different from the one obtained using analytical expression. Consequently, mass flow parameter and skew angle of PPSIM and VPSIM show slight differences in some cases, and affect the induced inflow distributions of these models.

4. VISCOUS VORTEX PARTICLE METHOD

A brief description of the Viscous Vortex Particle Model (VVPM) and its usage is covered here as full details are well documented in Refs. 16,17,18. VVPM solves for the vorticity field directly from the vorticity-velocity form of incompressible Navier-Stokes equations using a Lagrangian formulation. It involves solving the governing equations in a convection-diffusion process which applies to regions with vorticities only. In addition, it does not require any grid generation effort. VVPM captures the fundamental vorticity dominated flow physics for both vorticity stretching and diffusion due to airflow viscosity effect.

The VVPM rotor wake model is coupled with a lifting line based blade element model for vorticity source generation, which is directly related to blade bound circulation from the Kutta-Joukowski Theorem. This allows user-specified airloads distribution across the rotor disk, without the need for airfoil properties such as lift and drag coefficients. As such, this model can be used to extract finite state inflow modeling parameters for efficient analysis. Furthermore, VVPM is fully parallelized using both OpenMP on multi-core CPUs and CUDA on compatible GPUs, rendering it an extremely efficient high fidelity solution for vorticity dominated flow analysis.

5. SIMULATION SETUP

In this study, two tandem rotor configurations with different longitudinal separation distances are considered. The rotors are two bladed and have same geometries as Harrington coaxial rotor, Rotor-1[19]. The rotor radius is 12.5 ft and the rotational speed of upper/front and lower/back rotors is 37.5 rads/s. The upper/front and lower/back rotors of these tandem rotor configurations are vertically separated by a distance of 0.19R with no lateral separation. They are separated longitudinally by distances of 1.5R and 2.0R as shown in Figs. 1 and 2, respectively.

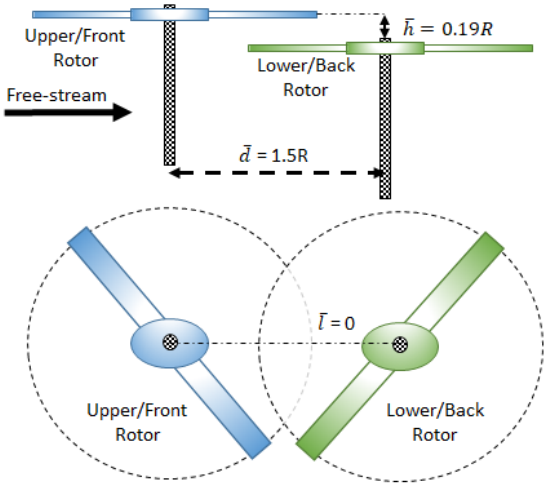

Figure 1: Configuration I

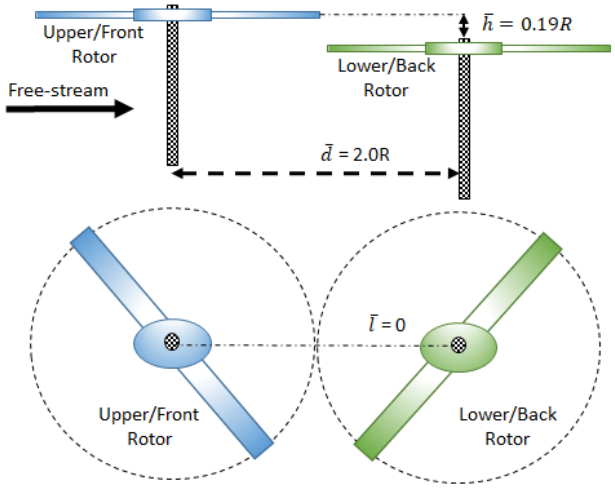

Figure 2: Configuration II

5.1. Simulation of VVPM

The established tandem rotor models are implemented in FLIGHTLAB[20]. The particle resolution is fixed at 3% of rotor radius and are distributed equally along the rotor blades. A script is used as a communication interface between FLIGHTLAB and VVPM. In the script, simulation parameters such as flight conditions and prescribed rotor loadings are specified.
Using the equation (9), the blade lift distribution, $L_q(\bar{r}, \bar{\psi}_q)$ is calculated from rotor pressure coefficients ($\tau_1^{0c}, \tau_2^{1c}, \tau_2^{1s}$). Then, blade bound circulation is known from Kutta-Joukowski Theorem and is used to compute the source vorticity in VVPM. By adopting this approach, induced inflows distribution at the rotor can be directly related to rotor loadings. Note that thrust (C_T) and moment coefficients (C_M, C_L) are related to the pressure coefficients in equation (9) by some constants[1].

$$
\begin{aligned}
L_{q1}^{0c}(\bar{r}, \bar{\psi}_q) &= \frac{2\pi}{Q}\rho\Omega^2 R^3 \tau_1^{0c} \bar{r}\sqrt{1-\bar{r}^2}\Psi_1^0 \\
L_{q2}^{1c}(\bar{r}, \bar{\psi}_q) &= \frac{2\pi}{Q}\rho\Omega^2 R^3 \tau_2^{1c} \bar{r}\sqrt{1-\bar{r}^2}\Psi_2^1 \cos(m\bar{\psi}_q) \\
L_{q2}^{1s}(\bar{r}, \bar{\psi}_q) &= \frac{2\pi}{Q}\rho\Omega^2 R^3 \tau_2^{1s} \bar{r}\sqrt{1-\bar{r}^2}\Psi_2^1 \sin(m\bar{\psi}_q)
\end{aligned} \tag{9}
$$

where

$$
\Psi_n^m(\nu) = \frac{\bar{P}_n^m(\nu)}{\nu}
$$

In FLIGHTLAB-VVPM model, each rotor has a total of 1440 sampling points distributed across the rotor plane at 30 radial and 48 azimuthal locations. At each time step, downwash and loading at these locations are sampled simultaneously and saved in memory before dumping them into an output file at the end of the simulation run. Rotor induced inflows are generated using the procedure summarized below.

1. Load a multi-rotor model into FLIGHTLAB scope environment
2. Define flight advance ratio and prescribed loadings on all rotors
3. Run the FLIGHTLAB-VVPM model until it achieves steady-state condition
4. Save time histories of variables such as blade loadings and induced velocities at pre-defined flow sampling points into an output file

5.2. Simulation of PPSIM and VPSIM

In all flight conditions, PPSIM and VPSIM use same prescribed rotor loadings as VVPM to solve the governing inflow equations given for PPSIM in equation (1) and VPSIM in equation (5). Both tandem rotor inflow models are time marched until they reach the steady-state condition. During the simulation, induced velocities are sampled at the rotor planes using 30 radial and 48 azimuthal locations for each rotor. In this study, higher number of states are selected to have an inflow distribution comparable to VVPM. As such, PPSIM uses 15 odd inflow states while VPSIM uses 15 odd and 15 even number of velocity states. In VPSIM, even numbered states are used for off-disk inflow calculation. It is important to note that even numbered velocity states have negligible impact on the on-disk inflow prediction, therefore 15 odd numbered inflow states in PPSIM are comparable to 15 odd and 15 even velocity states used in VPSIM . On the other hand, 15 even numbered velocity states have substantial effect on the off-disk inflow calculation.
In the simulations, both upper/front and lower/back rotors have thrust coefficient of 0.0035 while roll moment and pitch moment coefficients are fixed to zero for all flight conditions.

6. RESULTS AND ANALYSIS

In the current study, steady-state inflow distributions of two different tandem rotor configurations are calculated at hover and different advance ratios up to 0.20. The qualitative comparison has been made among PPSIM, VPSIM and VVPM by providing contour plots of induced flow distributions at each flight condition. For quantitative comparison, uniform (λ_0), fore-to-aft (λ_{1c}) and side-to-side (λ_{1s}) linear inflow variations are extracted from the rotor inflow distributions.
The induced velocity at the rotor disk due to mean (C_T) and cyclic loadings (C_M, C_L) can be expanded up to the uniform and first harmonic terms as,

$$
\bar{v}_z(\bar{r}, \psi) = \lambda_0 + \lambda_{1c}\bar{r}\cos(\psi) + \lambda_{1s}\bar{r}\sin(\psi) \tag{10}
$$

By using the orthogonal property of trigonometric functions, induced inflow variations in equation (10) is found to be[21],

$$
\begin{aligned}
\lambda_0 &= \frac{1}{\pi}\int_0^{2\pi}\int_0^1 \bar{v}_z(\bar{r}, \bar{\psi})\bar{r}\, d\bar{r}\, d\psi \\
\lambda_{1c} &= \frac{4}{\pi}\int_0^{2\pi}\int_0^1 \bar{v}_z(\bar{r}, \bar{\psi})\bar{r}^2\cos(\psi)\, d\bar{r}\, d\psi \\
\lambda_{1s} &= \frac{4}{\pi}\int_0^{2\pi}\int_0^1 \bar{v}_z(\bar{r}, \bar{\psi})\bar{r}^2\sin(\psi)\, d\bar{r}\, d\psi
\end{aligned} \tag{11}
$$

In equation (11), $\bar{r}$ and $\bar{\psi}$ are the rotor radial and azimuthal location, respectively of the sampled downwash, $\bar{v}_z$.
In this study, quantities related to upper/front rotor are bracketed with subscript 'U', i.e. $(\ )_U$. Similarly, lower/back rotor variables bracketed with subscript 'L', i.e. $(\ )_L$. For example, $(\lambda_0)_U$ and $(\lambda_0)_L$ correspond to upper/front and lower/back rotors uniform inflow component, respectively.
After extracting the linear inflow variations, flapping angles of upper/front and lower/back rotors are compared to further analyze the effect of inflow distribution.

6.1. Comparison of inflow distributions for configuration I

The comparison of upper/front and lower/back rotors steady-state extracted inflow distributions are given in Figs. 3 and 4, respectively. Figure 3 shows that models have good correlation at upper/front rotor $(\lambda_0)_U$ except the hover condition. PPSIM and VPSIM slightly overestimate the hover value of $(\lambda_0)_U$. In hover, VVPM has large upwash region near the blade tip as shown in Figs. 5 and 6. Because of this large upwash region, VVPM has smaller $(\lambda_0)_U$ than PPSIM and VPSIM. This discrepancy among the models can be alleviated by correcting the uniform inflow component of inflow influence coefficient matrix, $[L]$. As speed increases, $(\lambda_0)_U$ of each model is rapidly decreasing like a single rotor momentum theory inflow (Figs. 3 &5). This is expected since upper/front rotor is not under direct influence of the lower/back rotor wake.
The predictions of $(\lambda_{1c})_U$ indicate that PPSIM and VPSIM are able to follow the trend throughout all flight conditions. PPSIM and VPSIM have excellent correlation with VVPM at higher speeds while having some differences in low advance ratio region. At low speeds, magnitude of the wake is comparable to flight speed and wake structure becomes highly nonlinear. The wake travel longer along the front region of rotor due to wake distortion effects before it convects downstream. These nonlinear wake distortion effects are not included in PPSIM and VPSIM formulation as their wake geometry assumes averaged momentum rigid wake, and both front and rear side of the rotor use same skew angle. Figure 5 qualitatively presents that VVPM has larger upwash region (causing fore-to-aft inflow gradient) than PPSIM and VPSIM at the advance ratios of 0.04 and 0.07. As speed increases, difference between VVPM and finite state tandem rotor inflow models diminishes quickly. The $(\lambda_{1c})_U$ difference at the low speed region can be improved modifying fore-to-aft and uniform to fore-to-aft coupling components in

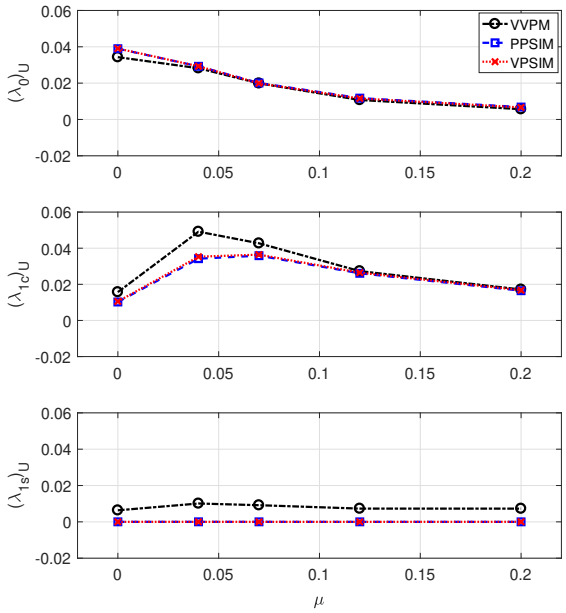

Figure 3: Upper/front rotor linear inflow variations, configuration I

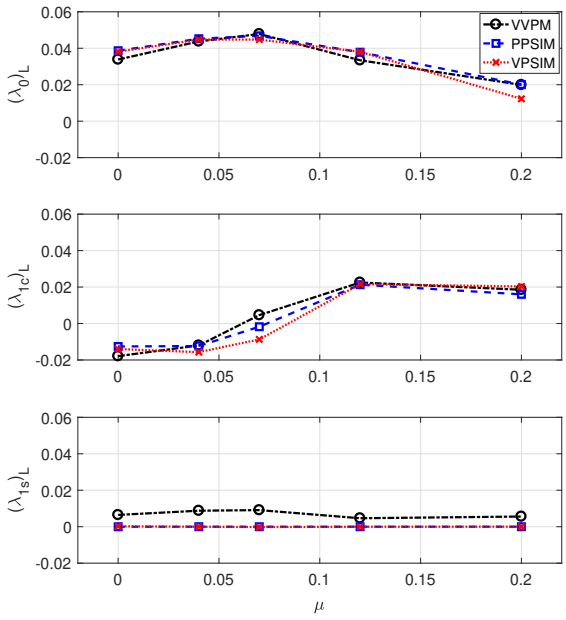

Figure 4: Lower/back rotor linear inflow variations, configuration I

the inflow influence coefficient matrix, $[L]$.
The estimations of $(\lambda_{1s})_U$ shows that there is almost a constant difference between VVPM and finite state multi-rotor models. This difference is due to swirl of the velocity considered in VVPM. Although this difference is small, correlation can be

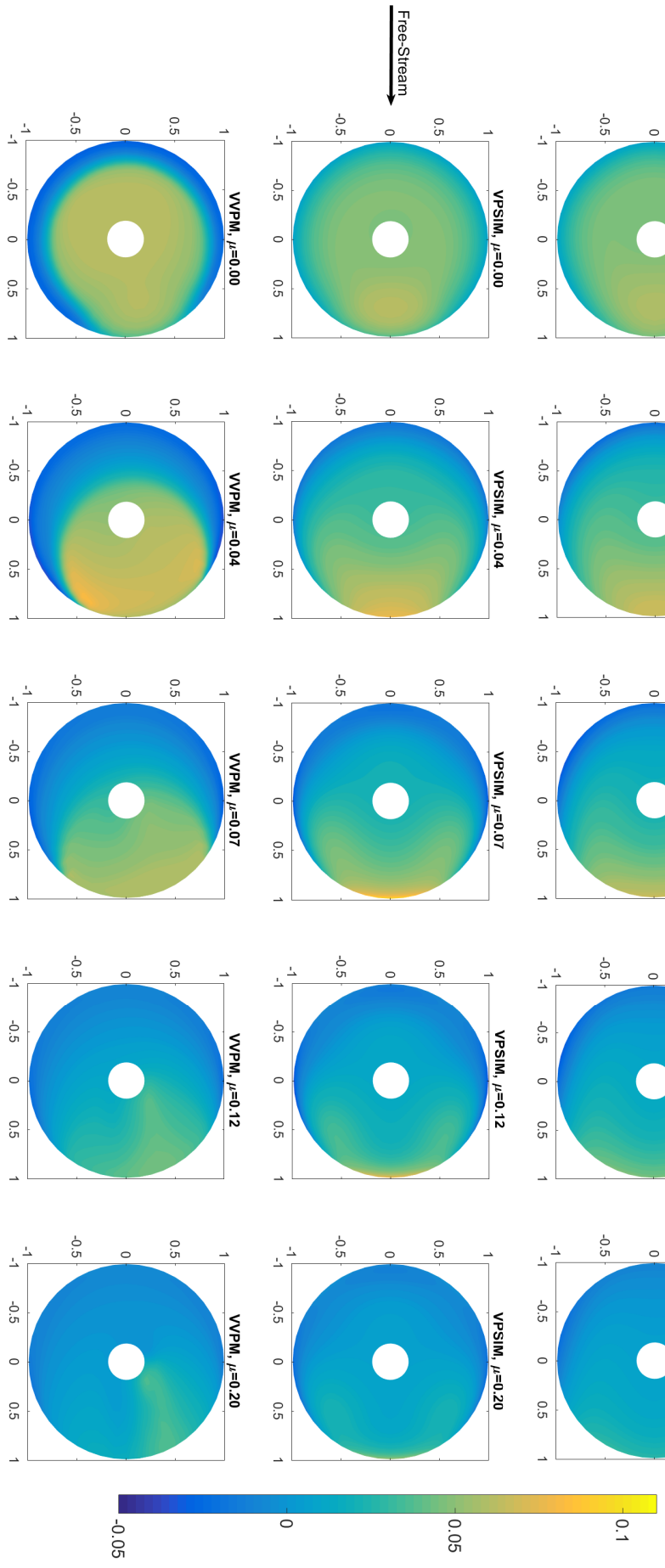

Figure 5: Upper/front rotor inflow distributions vs. advance ratio, configuration I

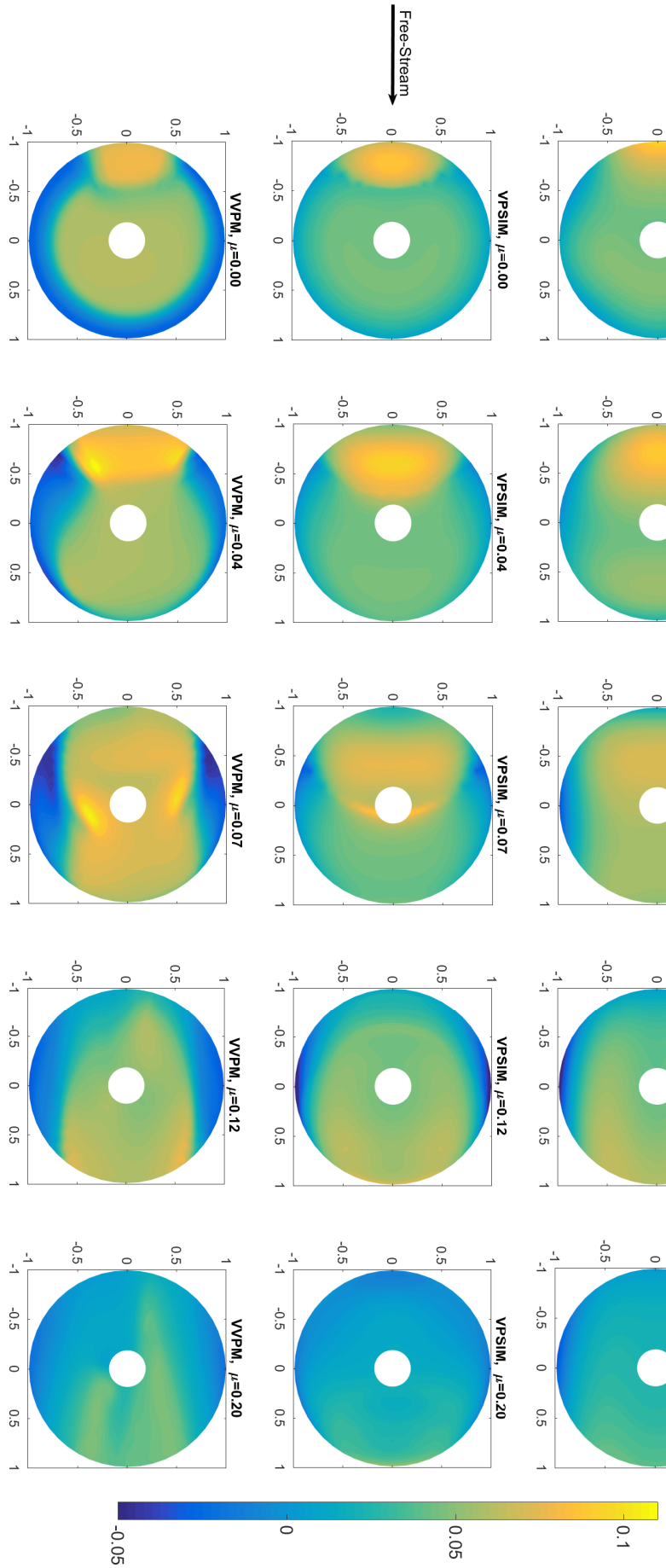

Figure 6: Lower/back rotor inflow distributions vs. advance ratio, configuration I

improved by adding swirl term into $[L]$.

Figure 4 presents the lower/back rotor extracted inflow coefficients. The $(\lambda_0)_L$ predictions of PPSIM and VPSIM have overall good agreement with VVPM data. Unlike the upper/front rotor case, $(\lambda_0)_L$ first increases up to advance ratio of 0.07, then reduces as speed increases further. Although upper/front rotor inflow rapidly decreases with speed, increase in the interference region at lower/back rotor compensates this reduction as shown in Fig. 6. This increase in the interference area is accurately captured by PPSIM and VPSIM. At the highest advance ratio where skew angle is close to $90°$, VPSIM underestimates the value of $(\lambda_0)_L$ compared to VVPM and PPSIM. It is because off-disk velocity estimation of VPSIM has poor convergence towards the pure edgewise flow condition ($\chi \geq 85°$), however this problem can be solved using the so called 'blended method'[15].

The estimation of $(\lambda_{1c})_L$ shows completely different trend than the $(\lambda_{1c})_U$. In configuration I, lower/back rotor's front region partially overlaps with upper/front rotor, and operates under the wake of upper/front rotor even in hover. The downwash received from the upper/front rotor creates an $(\lambda_{1c})_L$ with opposite sign of $(\lambda_{1c})_U$ as shown in Fig. 6. The change in the $(\lambda_{1c})_L$ is insignificant as speed increases from hover to advance ratio of 0.04 (Fig. 4). Then, $(\lambda_{1c})_L$ starts to increase and becomes comparable to $(\lambda_{1c})_U$ after the advance ratio of 0.12. Both PPSIM and VPSIM are able to capture the variation in $(\lambda_{1c})_L$ compared to VVPM throughout the flight envelope. The only noticeable difference is seen at advance ratio of 0.07 where $(\lambda_{1c})_L$ changes sign.

Similar to the upper/front rotor case, PPSIM and VPSIM do not show any variation in $(\lambda_{1s})_L$ as presented in Fig. 4. The correlation can be improved using adding swirl terms to inflow influence coefficient matrix.

6.2. Comparison of inflow distributions for configuration II

In this configuration, longitudinal separation distance is increased from 1.5R to 2.0R. The extracted linear inflow coefficients are given for upper/front and lower/back rotors in Figs. 7 and 8, respectively. The upper/front rotor inflow predictions (Fig. 7) of configuration II show similarity with the upper/front rotor inflow predictions obtained in configuration I (Fig. 3). Only noticeable magnitude differences of $(\lambda_0)_U$ and $(\lambda_{1c})_U$ are seen in hover where configuration I has partially overlapping region. The upper/front rotor induced inflow distributions are given in Fig. 9. It is seen that coupling is insignificant in hover as inflow distributions of configuration II clearly differs from the configuration I (Fig. 5).

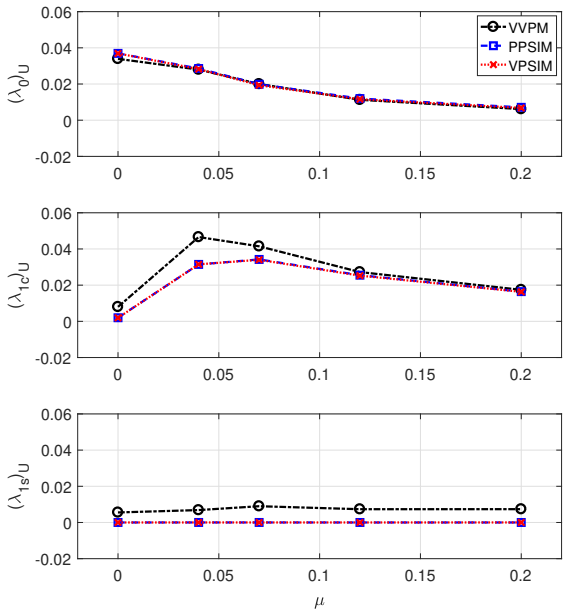

Figure 7: Upper/front rotor linear inflow variations, configuration II

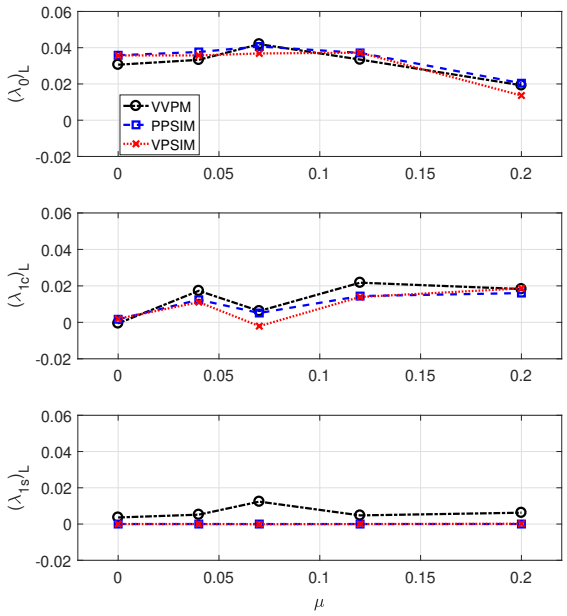

Figure 8: Lower/back rotor linear inflow variations, configuration II

Figure 8 presents lower/back rotor extracted inflow coefficients. The $(\lambda_0)_L$ shows, PPSIM and VPSIM

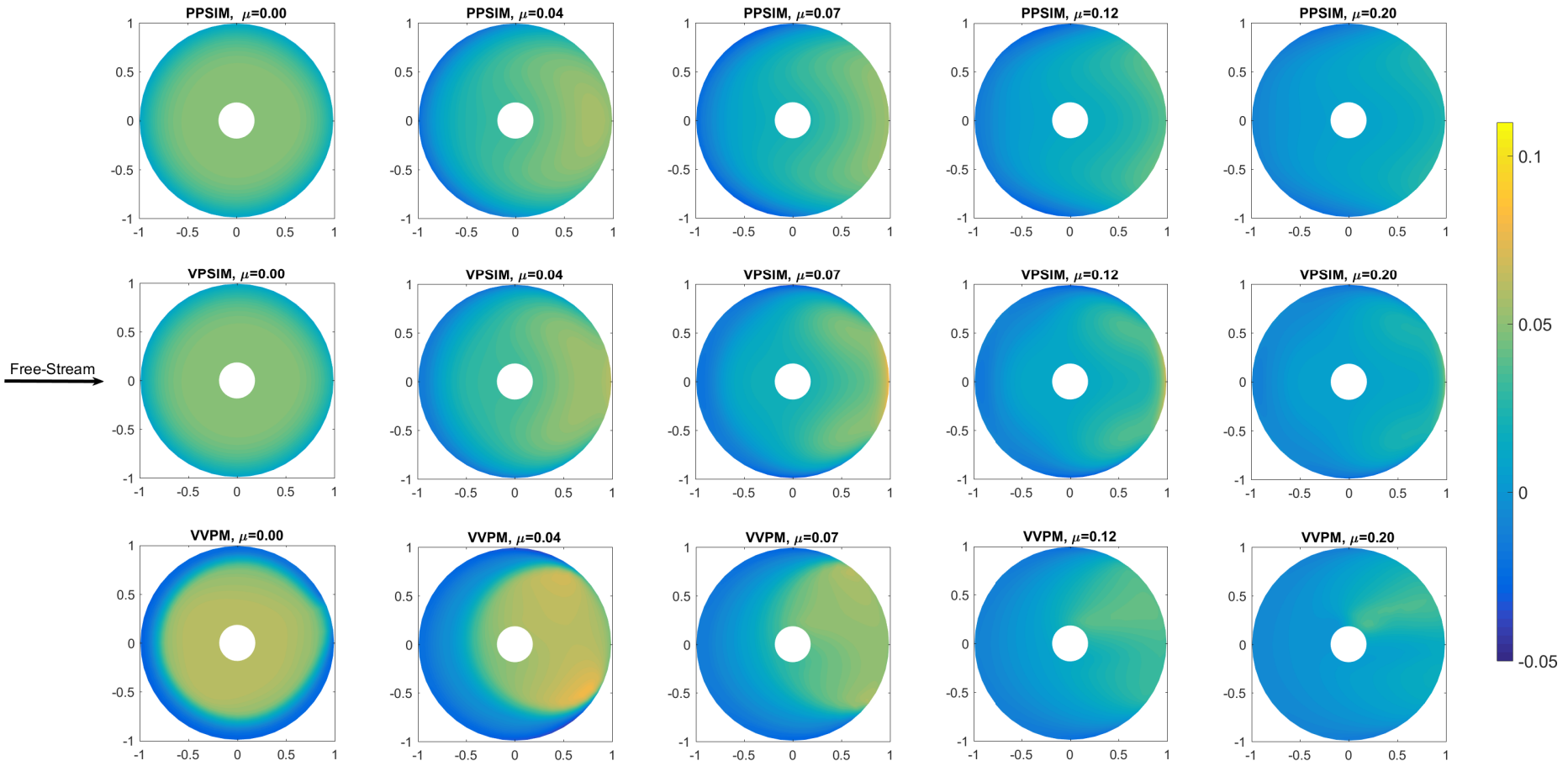

Figure 9: Upper/front rotor inflow distributions vs. advance ratio, configuration II

Presented at 44th European Rotorcraft Forum, Delft, The Netherlands, 19–20 September, 2018.

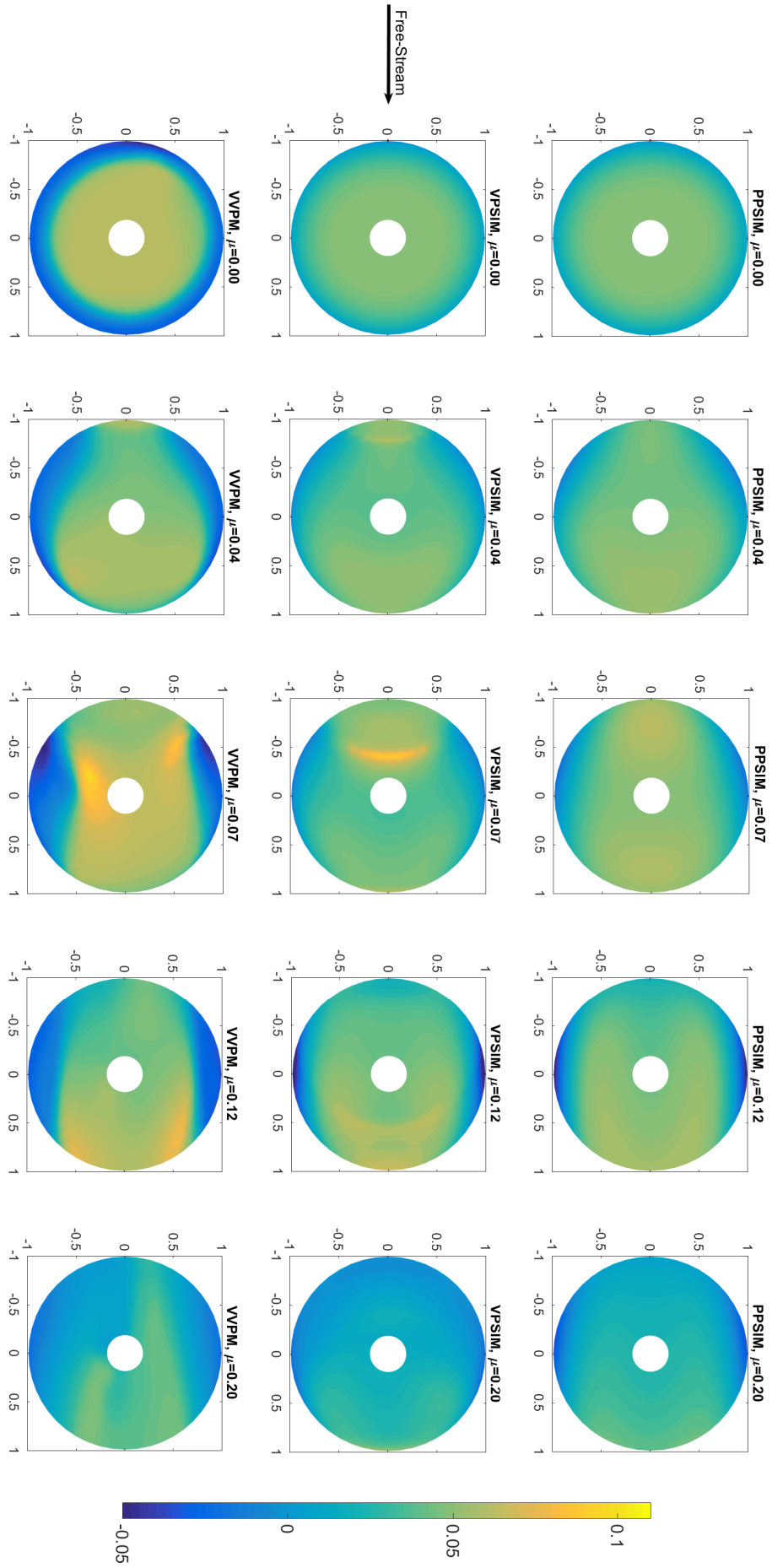

Figure 10: Lower/back rotor inflow distributions vs. advance ratio, configuration II

have good correlation with VVPM for all flight conditions. The slight overestimation of $(\lambda_0)_L$ in hover is due to excessive upwash region near the blade tip predicted by VVPM. At upper/front rotor, uniform inflow component ($(\lambda_0)_U$) is rapidly diminished while at lower/back rotor $(\lambda_0)_L$ slightly increases indicating growth of interference region up to advance ratio of 0.07, then $(\lambda_0)_L$ decreases at higher advance ratios. Although $(\lambda_0)_L$ becomes smaller at the advance ratio of 0.20, it is still significantly larger (2-3 times) than $(\lambda_0)_U$.

Next, Fig. 8 shows that fore-to-aft inflow gradient ($(\lambda_{1c})_L$) first increases from hover as advance ratio increases, then decreases, and after that, increases again. These changes can be also qualitatively spotted in contour plots (Fig. 10). This trend in $(\lambda_{1c})_L$ prediction is captured by both PPSIM and VPSIM although there are small differences compared to VVPM.

Similar to other cases, both PPSIM and VPSIM predict $(\lambda_{1s})_L$ as zero due to lack of swirl coupling. VVPM has negligible $(\lambda_{1s})_L$ predictions except at the advance ratio of 0.07 where coupling between upper/front and lower/back rotors becomes maximum.

6.3. Effect of inflow distribution on flapping angles

In this section, the effects of inflow distribution on upper/front rotor and lower/back rotor flapping angles are analyzed. It is shown that[22] fore-to-aft inflow gradient directly affects the lateral flapping angle estimations. In the selected tandem rotor configurations, upper/front and lower/back rotors have significantly different fore-to-aft inflow gradients which suggest investigation of flapping angles. The flapping angles play a key role for handling qualities analyses and control law development since they are directly related to collective, θ_0, lateral, θ_{1c} and longitudinal, θ_{1s} cyclic controls.

The lateral (β_{1s}) and longitudinal (β_{1c}) flapping angles are calculated as follow[22],

$$\beta_{1c} = -2\mu^2(\alpha_s - \theta_{1s}) + \frac{16\mu}{a}\frac{C_T}{\sigma} + 2\mu\lambda_0 - \theta_{1s} - \frac{8}{2\pi}\int_0^{2\pi}\int_0^1 \lambda(\bar{r},\psi)(\bar{r}^2 sin\psi + \bar{r}\mu sin^2\psi) \quad (12)$$

$$\beta_{1s} = \frac{4}{3}\mu\beta_0 + \theta_{1c} + \frac{8}{2\pi}\int_0^{2\pi}\int_0^1 \lambda(\bar{r},\psi)\times (\bar{r}^2 cos\psi + \bar{r}\mu sin\psi cos\psi) \quad (13)$$

where α_s is shaft tilt angle, a is lift curve slope and σ stands for the solidity. In equations (12) and (13), θ_{1c}, θ_{1s} and α_s are taken as zero. The last term in equation (12) is added to account for lateral inflow distribution, because it was neglected in the original formulation[22]. Lastly, in the flapping angle calculations, only extracted inflow components (λ_0, λ_{1c}, λ_{1s}) are used. Note that lateral (β_{1s}) and longitudinal (β_{1c}) flapping angles obtained using VVPM are considered as 'true' values.

Figure 11 presents lateral flapping angle estimations of configuration I. As expected, upper/front and lower/back rotors' lateral flapping angles have direct relation to their respective fore-to-aft inflow gradients. The $(\beta_{1s})_U$ predictions show approximately one degree difference between VVPM and finite state models at advance ratio of 0.04. At this speed, wake distortion effects in VVPM are maximum, and creating an excessive fore-to-aft inflow gradient. The $(\beta_{1s})_U$ predictions of PPSIM and VPSIM match well with VVPM at other flight conditions. Lower/back rotor $(\beta_{1s})_L$ estimations at low speed region have entirely different trend from $(\beta_{1s})_U$. The $(\beta_{1s})_L$ has negative value at hover and slowly increases as advance ratio is increased. Unlike the upper/front rotor or single rotor case[22], $(\beta_{1s})_L$ does not have a peak at low advance ratio region. This is due to the fore-aft inflow variation that is remarkably different from the upper/front rotor. As shown in Fig. 6, leading downwash, instead of the upwash as with the upper/front rotor, can be seen over the lower/back rotor plane at low speed, which causes the lower/back rotor flap to the port side. These differences in magnitude and trend of upper/front and lower/back rotors' lateral flapping angles might be important for control law development. PPSIM and VPSIM provide accurate estimations of these angles.

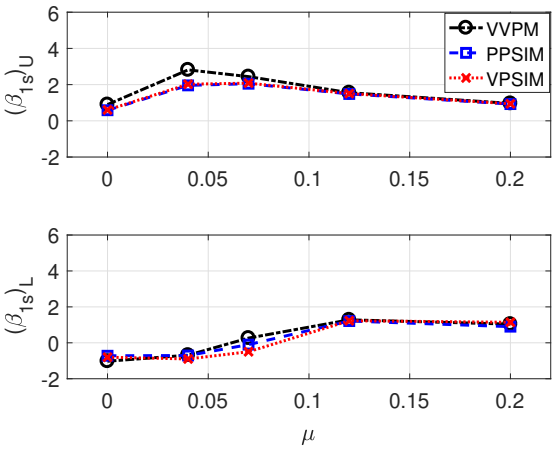

Figure 11: Lateral flapping angle predictions, configuration I

The longitudinal flapping estimation of configuration I is given in Fig. 12. PPSIM and VVPM have good correlation with VVPM at all flight conditions. The approximately constant and small difference in the flapping angle is attributed to lateral inflow gradient (λ_{1s}) predictions. Both $(\beta_{1c})_U$ and $(\beta_{1c})_L$ have linear trend captured by PPSIM and VPSIM.

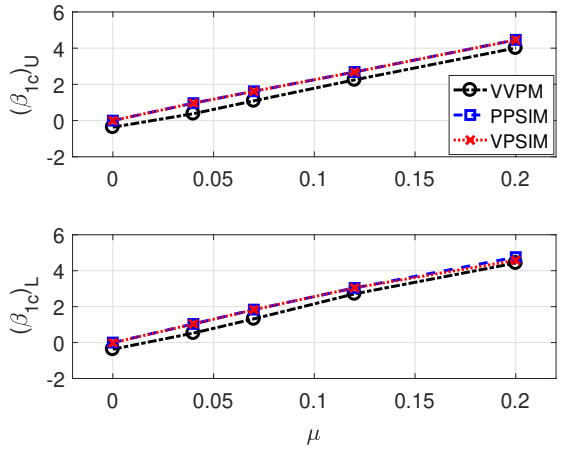

Figure 12: Longitudinal flapping angle predictions, configuration I

Next, lateral flapping angle predictions of configuration II are shown in Fig. 13. Upper/front rotor lateral flapping angle estimation ($(\beta_{1s})_U$) of configuration II is similar (except hover) to $(\beta_{1s})_U$ obtained for configuration I. This is expected since upper/front rotor does not operate under direct wake of lower/back rotor. At lower/back rotor, $(\beta_{1s})_L$ predictions are slightly different from the one obtained for configuration I due to different interference regions. Unlike the upper/front rotor case, $(\beta_{1s})_L$ stays close to zero at low advance ratio region due to wake convected from upper/front rotor. After advance ratio of 0.12, both $(\beta_{1c})_U$ and $(\beta_{1c})_L$ become closer to each other indicating that effect of upper/front rotor wake becomes smaller.

7. CONCLUDING REMARKS

Finite state inflow models for tandem rotor configurations have been developed using the pressure potential and velocity potential superposition approaches. Previously identified physical wake effects such as wake contraction and viscous dissipation are added to PPSIM and VPSIM. The formulation of mass flow parameter in VPSIM is revisited to have a formulation closer to classical mass flow parameter equation used in PPSIM. With the new mass flow parameter matrix in VPSIM, it is shown that VPSIM and PPSIM converge to similar steady-state values.

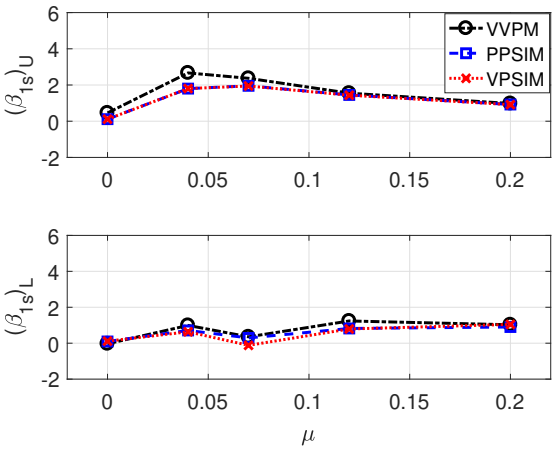

Figure 13: Lateral flapping angle predictions, configuration II

The PPSIM and VPSIM are compared against a more comprehensive viscous Vortex Particle Method using two tandem rotor configurations with different longitudinal separation distances. Comparisons cover a flight range from hover to advance ratio of 0.20. This study limits the inflow variations to uniform, fore-to-aft and side-to-side inflow components for quantitative comparison. In addition, inflow distributions over the rotor disks are provided for qualitative analysis. Differences among the models such as excessive upwash region in hover, distortion of wake at low advance ratios and uniform to side-to-side and fore-to-aft to side-to-side inflow couplings due to swirl velocities are identified. Despite these differences, PPSIM and VPSIM correlate well with VVPM at all flight conditions. Lastly, effect of inflow variations on flapping angles are studied. It is seen that upper/front and lower/back rotors have significantly different lateral flapping angles at low speeds whereas longitudinal flapping angle predictions of both rotors show similarity and linear in trend like single rotor. PPSIM and VPSIM accurately capture these differences in flapping angles.
Next step is to incorporate identified corrections such as upwash region near the blade tip, distortion of wake and swirl coupling in PPSIM and VPSIM for improved correlation.

8. ACKNOWLEDGMENTS

This study is supported under the NRTC Vertical Lift Rotorcraft Center of Excellence (VLRCOE) from the U.S. Army Aviation and Missile Research, Development and Engineering Center (AMRDEC) under Technology Investment Agreement W911W6-17-2-0002, entitled Georgia Tech Vertical Lift Research

Center of Excellence (GT-VLRCOE) with Dr. Mahendra Bhagwat as the Program Manager. The authors would like to acknowledge that this research and development was accomplished with the support and guidance of the NRTC. The views and conclusions contained in this document are those of the authors and should not be interpreted as representing the official policies, either expressed or implied, of the AMRDEC or the U.S. Government. The U.S. Government is authorized to reproduce and distribute reprints for Government purposes notwithstanding any copyright notation thereon.

REFERENCES

[1] C. He, *Development and Application of a Generalized Dynamic Wake Theory for Lifting Rotors*. PhD thesis, Georgia Institute of Technology, July 1989.

[2] D. Peters and C. He, "Correlation of Measured Induced Velocities with a Finite-State Wake Model," *Journal of the American Helicopter Society*, vol. 36, 1991.

[3] J. Morillo and D. A. Peters, "Velocity Field above a Rotor Disk by a New Dynamic Inflow Model," *Journal of Aircraft*, vol. 39, pp. 731–738, Oct. 2002.

[4] J. V. R. Prasad, M. Nowak, and H. Xin, "Development of a Finite State Model for a Coaxial Rotor in Hover," in *Proceedings of the 38th European Rotorcraft Forum*, Sept. 2012.

[5] M. Nowak, J. V. R. Prasad, H. Xin, and D. A. Peters, "A Potential Flow Model for Coaxial Rotors in Forward Flight," in *Proceedings of the 39th European Rotorcraft Forum, Moscow, Russia*, Sept. 2013.

[6] M. Nowak, J. V. R. Prasad, and D. Peters, "Development of a Finite State Model for a Coaxial Rotor in Forward Flight," in *Proceedings of the AHS 70th Annual Forum*, May 2014.

[7] J. V. R. Prasad, Y. B. Kong, and D. A. Peters, "Analytical Methods for Modeling Inflow Dynamics of a Coaxial Rotor System," in *Proceedings of the 42nd European Rotorcraft Forum, Lille, France*, Sept. 2016.

[8] Y. B. Kong, J. V. R. Prasad, L. N. Sankar, and J. Kim, "Finite State Coaxial Rotor Inflow Model Improvements via System Identification," in *Proceedings of the AHS 72nd Annual Forum, West Palm Beach, Florida*, May 2016.

[9] Y. B. Kong, J. V. R. Prasad, and D. A. Peters, "Development of a Finite State Dynamic Inflow Model for Coaxial Rotor using Analytical Methods," in *Proceedings of the AHS 73rd Annual Forum*, May 2017.

[10] Y. B. Kong, J. V. R. Prasad, and D. A. Peters, "Analysis of a Finite State Multi-Rotor Dynamic Inflow Model," in *Proceedings of the 43rd European Rotorcraft Forum*, Sept. 2017.

[11] F. Guner, Y. B. Kong, J. V. R. Prasad, D. Peters, and C. He, "Development of Finite State Inflow Models for Multi-Rotor Configurations using Analytical Approach," in *Proceedings of the 74th Annual Forum*, May 2018.

[12] C. He and J. Zhao, "Modeling Rotor Wake Dynamics with Viscous Vortex Particle Method," *AIAA Journal*, vol. 47, 2009.

[13] C. He, H. Xin, and M. Bhagwat, "Advanced Rotor Wake Inteference Modeling for Multiple Aircraft Shipboard Landing Simulation," in *American Helicopter Society 59th Annual Forum*, June 2004.

[14] Z. Fei, *A Rigorous Solution for Finite-State Inflow throughout the Flowfield*. PhD thesis, Washington University in St. Louis, May 2013.

[15] J. Huang, *Potential-flow Inflow Model Including Wake Distortion and Contraction*. PhD thesis, Washington University in St. Louis, May 2015.

[16] C. He and J. Zhao, "A Real Time Finite State Induced Flow Model Augmented with High Fidelity Viscous Vortex Particle Simulation," in *Proceedings of the AHS 64th Annual Forum*, May 2008.

[17] J. Zhao and C. He, "Real-Time Simulation of Coaxial Rotor Configurations with Combined Finite State Dynamic Wake and VPM," in *Proceedings of the AHS 70th Annual Forum*, May 2014.

[18] C. He, M. Syal, M. B. Tischler, and O. Juhasz, "State-space Inflow Model Identification from Viscous Vortex Particle Method for Advanced Rotorcraft Configurations," in *Proceedings of the 73rd Annual Forum*, May 2017.

[19] R. Harrington, "Full Scale Tunnel Investigation of the Static Thrust Performance of a Coaxial Helicopter Rotor," NACA TN 2318, Mar. 1951.

[20] Advanced Rotorcraft Technology, Inc., *FLIGHTLAB X-Analysis user manual*, July 2013.

[21] J. Zhao, *Dynamic Wake Distortion Model for Helicopter Maneuvering Flight*. PhD thesis, Georgia Institute of Technology, Mar. 2005.

[22] F. D. Harris, "Articulated Rotor Blade Flapping Motion at Low Advance Ratio," *Journal of the American Helicopter Society*, vol. 17, pp. 41–48, Jan. 1972.